PROCEEDINGS of
CHEF 2013

Precision calibration of the DØ liquid argon calorimeter and algorithms of electron, photon and jet reconstruction

Jan Stark[*†]
LPSC Grenoble, Université Joseph Fourier Grenoble 1, CNRS/IN2P3 (France)
E-mail: stark@in2p3.fr

During Run II of the Tevatron, the DØ calorimeter had to operate under much more difficult conditions than during Run I. This lead to significant challenges, some of which were expected and others were not. The main challenges are due to the large instantaneous luminosity in Run II (which results in a shorter integration time and larger pile-up) and the large increase of the amount of uninstrumented material in front of the calorimeter. We summarise some of these challenges and the solutions that have been implemented to overcome them. The energy resolution achieved in Run II is necessarily not quite as good as in Run I, but it is still consistent with the physics goals. More importantly, calorimeter energy scales for all kinds of objects (including the dependence on instantaneous luminosity etc) are precisely quantified and understood. This is one of the bases of the rich collection of physics results from DØ in Run II.

Calorimetry for High Energy Frontiers - CHEF 2013,
April 22-25, 2013
Paris, France

[*]Speaker.
[†]For the DØ Collaboration..

1. Introduction

Data taking at the Fermilab Tevatron has recently been completed. There were two main data taking periods. The first one is called Run I and it ended in 1996. One of the main physics results of Run I was the observation of the top quark, which was jointly announced by CDF and DØ (the two experiments at the Tevatron) in 1994. The second data taking period, referred to as Run II, started in 2001 and was completed in September 2011. Many of the final physics results based on the full Run II dataset are available, and a number of precision measurements based on the full dataset are nearing completion. In these proceedings, we describe the Run II experience with precision energy measurements based on the DØ calorimeter. Precise energy measurements from the calorimeter are a key ingredient in many of the salient physics results from Run II of DØ. Two examples include precise measurements of the top quark mass (m_t) and of the W boson mass (M_W). Measurements of these two masses are key inputs to tests of the consistency of the standard model (SM) of particle physics. In the context of this model, M_W can be expressed as

$$M_W = \sqrt{\frac{\pi\alpha}{\sqrt{2}G_F}}\frac{1}{\sin\theta_W\sqrt{1-\Delta r}}\,, \tag{1.1}$$

where G_F is the Fermi weak coupling, α is the is the EM coupling at the renormalisation energy scale $Q = M_Z$, and θ_W is the weak mixing angle. The term Δr includes all radiative corrections, i.e. $\Delta r = 0$ corresponds to the tree level result. The radiative corrections include contributions from loops including top quarks and loops including a Higgs boson. Given that the other quantities in Eq. 1.1 are well known, this equation can be interpreted as a relation between the masses of the W boson, the top quark and the SM Higgs boson. In extensions to the SM (like e.g. the MSSM), additional contributions to Δr appear. Given precise measurements of the masses of the W boson and the top quark, Eq. 1.1 provides indirect constraints on the Higgs boson mass from internal consistency of the SM. The current situation, using the precise measurements of m_t from the Tevatron and the world average for M_W is summarised in Fig. 1(a). The measurements included in the world average M_W are summarised in Fig. 1(b). This world average is driven by the results from the Tevatron. The the mass (measured directly) of new boson discovered in 2012 at CERN [1,2] is inside the blue band in Fig. 1(a), i.e. consistent with the indirect constraints from the SM.

The DØ detector in Run II [7] has been extensively upgraded compared to Run I. The calorimeter itself is the same in both Runs, only the associated read-out electronics have been replaced in Run II to accommodate the significantly shorter integration time and larger event rate in Run II. But the environment in which the calorimeter has to operate has changed dramatically in Run II. This lead to new challenges which had to be addressed. Selected examples of these challenges as well as the solutions that have been implemented to overcome them (and make the rich set of physics results, including the measurements discussed above, possible) are discussed in the following sections.

2. Calorimeter gain calibrations

At the start of data taking during Run II, it became clear that the energy response of the calorimeter was rather non-uniform, i.e. a given read-out cell could show a deviation from the

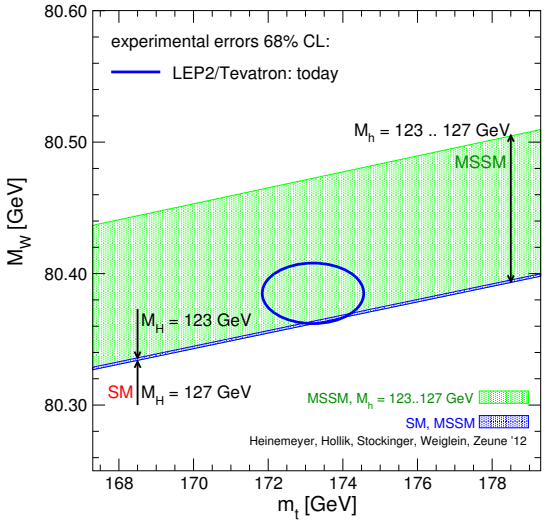

(a) Comparison of direct and indirect constraints on the Higgs boson mass. Taken/updated from Refs. [3–5], including two-loop corrections for the precision observables cited therein.

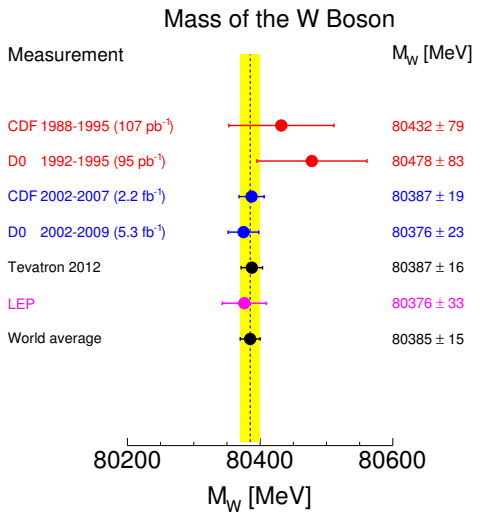

(b) Current world average value of direct measurements of the W boson mass [6].

Figure 1: Comparison of indirect and direct constraints on the Higgs boson mass (a) and contributions to the world average mass of the W boson (b) that is used in this comparison.

expected gain that was very different from neighbouring cells. Small gain non-uniformities had been observed in Run I as well, and they were explained by effects like small non-uniformities in the thickness of the uranium absorber plates caused by the finite mechanical precision in their production. But the non-uniformities observed at the start of Run II (up to 20 % in some parts of the central EM calorimeter) were much larger than during Run I, which was not expected. The initial tests of the energy response and uniformity were based on studies of the position of the mass peak in $Z \to e^+e^-$ events and the distribution of E/p for electrons from $W \to e\nu$ decays. While these processes, in particular $Z \to e^+e^-$, provide powerful control samples for calorimeter energy scale studies, their production cross section is small, and control samples therefore suffer from limited statistics. The observable E/p can be used to study the energy measurements E provided that the momentum measurements p from the central tracking system are well understood. At the start of Run II, the magnetic central tracking system of DØ was completely new and also needed to be commissioned *in situ*. Futhermore, this new tracking system had to fit inside the existing calorimeter. Its radius is therefore small and the p resolution for electrons from Z or W decay is neccessarily significantly worse than the energy resolution. These limitations imply that a precise per-cell *in situ* gain calibration is not possible based on Z and W control samples only.

A precise gain calibration has been obtained by combining the technique called ϕ intercalibration with the constraints obtained from the position of the $Z \to e^+e^-$ mass peak. The idea of ϕ intercalibration is simple: given that the Tevatron beams are unpolarised, the energy flow produced in the collisions is expected to be symmetric in ϕ. Any observed asymmetries must be due to energy mismeasurements, and the gain calibrations can be adjusted to restore ϕ symmetry. In prac-

tice we compare, for the read-out cells in a ring at given pseudo-rapidity η, the event rates for per-cell energy deposits above a certain energy threshold. This can be done, e.g. using unbiased events collected by reading out the detector during randomly selected beam crossings (so-called "zero bias" (ZB) events). The main disadvantage of ZB events is the fact that the energy deposits in these events are typically small, and the ϕ intercalibration therefore needs to be performed at relatively low energies (low compared to the energies involved in the physics processes that we ultimately want to study). This makes the resulting calibration constants sensitive to the effect of non-uniformities in the distribution of uninstrumented material in front of the calorimeter, whereas our goal is to study the non-uniformities in the gains of the read-out cells of the calorimeter itself. We therefore implemented a dedicated trigger to collect events for ϕ intercalibration. It selects events which contain at least one read-out tower with a large energy deposit. This dedicated trigger was frequently enabled towards the end of Tevatron stores where significant amounts of bandwidth are available in the trigger system (due to the decrease of the rates of physics triggers). This is illustrated in Fig. 2(a). In the store shown at the bottom, the available bandwidth at the end of the store is filled up with events for ϕ intercalibration.

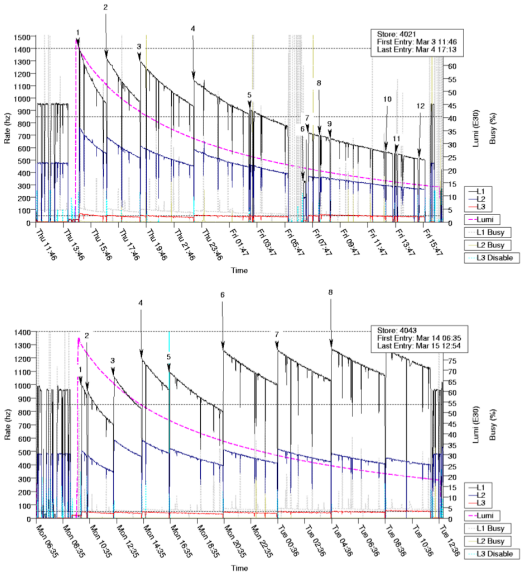

(a) DØ trigger rates for two Tevatron stores. Top: a typical store. Bottom: A store during which data for ϕ intercalibration have been collected.

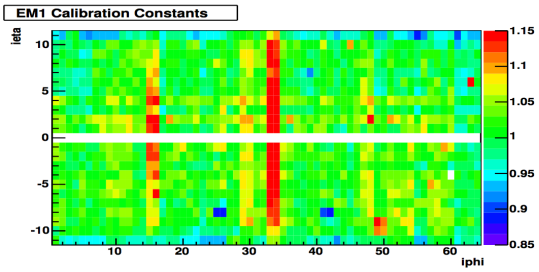

(b) Relative multiplicative gain calibration constants determined for the first read-out layer of the central EM calorimeter.

Figure 2: Illustration of the data taking strategy used to collect dedicated datasets for phi intercalibration, and example of relative gain correction constants obtained using ϕ intercalibration.

Figure 2(b) shows an example of ϕ intercalibration constants for the cells in the first layer of the central EM calorimeter (EM1). The indices ieta and iphi are used to number the cells. The band at iphi = 33, 34 which shows very large deviations from unity corresponds to one of the 32 phi modules of the central EM calorimeter. A photograph of part of the EM calorimeter is shown in

Fig. 3(a). The module that has been visibly deformed during installation is the one that covers iphi = 33, 34. Due to the deformation, a large pressure results on the signal board that is positioned in one of the two argon gaps of the EM1 section. Since the signal boards are not very rigid (as shown in Fig. 3(b)) and only loosely fixed in the middle of the argon gaps, this particular board suffers, over the entire length of the module, from displacements from the nominal position. This is an extreme example of a deformation, but due to the lack of rigidity, all signal boards in the calorimeter are only approximately positioned in the middle of the corresponding argon gap. In Run I this was not a problem, since the signal integration time was long compared to the drift time along the argon gaps: a displacement of the signal board simply reduces the amount of signal from the argon on one side of the board and increases the amount of signal from the other side of the board by the same amount. In Run II the integration time ($\sim$ 260 ns) is shorter than the drift time (450 ns), and any displacement of the signal board results in a reduction of the signal that is read out. The resulting gain non-uniformities are corrected using the results from ϕ intercalibration and studies of the position of the mass peak in $Z \to e^+e^-$, which is used to determine the relative energy scales of rings of readout cells at different ieta.

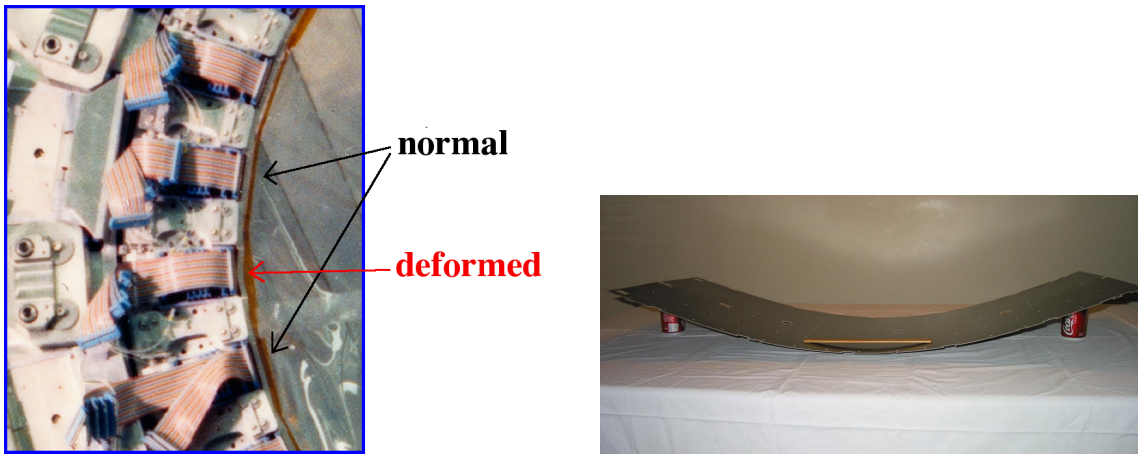

(a) Photograph of a section of the central EM calorimeter taken during assembly.

(b) Photograph of a spare signal board of the central fine hadronic calorimeter.

Figure 3: Photographs that illustrate the origin of the large outliers in the gain calibration constants which are shown in Fig. 2(b).

3. Effect and treatment of uninstrumented material

During Run I, the amount of material in front of the first active layer of the calorimeter was limited: it was dominated by the cryostat wall which represents 1.1 radiation lengths (X_0) of material in the case of the central calorimeter. In Run II, this amount has increased significantly. The increase is due to the new magnetic central tracking system and the addition of a pre-shower detector which could not be exploited for energy measurements. The tracking system itself represents only $0.1\,X_0$, but the superconducting solenoid that surrounds it adds $0.9\,X_0$ to the material budget.

A new pre-shower detector with a thickness of $1.3\,X_0$, including $1\,X_0$ of lead absorber plates, has been installed between the solenoid and the wall of the calorimeter cryostat. One of the design goals of the pre-shower detector was to be included in calorimetric energy measurements. Due to issues with the corresponding readout electronics (specifically a lower dynamic range than intended) that could only be mitigated late in Run II, the pre-shower detector is not used for this purpose. It is however used to improve the precision of the position measurements for calorimeter clusters (thanks to the relatively fine granularity of the pre-shower detector) and to optimise trigger decisions, at all three levels of the DØ trigger system.
Figure 4(a) illustrates how electron showers are sampled by the central calorimeter in Run II. It shows the average longitudinal profile of a shower initiated by an electron with $E = 45$ GeV (a typical electron from $Z \to e^+e^-$ decay), i.e. the average amount of energy deposited as a function of the depth in the DØ detector (starting at a depth of $0\,X_0$ at the interaction point, reaching almost $4\,X_0$ at the beginning of the first layer of the EM calorimeter [EM1], etc). As can be seen from this figure, the fraction of the electron energy deposited in the first X_0 of material is small. The situation was therefore very favourable in Run I. In Run II, the first $\sim 4\,X_0$ are uninstrumented from the point of view of calorimetry, and the average fraction of energy that is not visible to the calorimeter system is appreciable. Fluctuations from one electron shower to another are also important. To illustrate this point, we also show different simulated shower profiles in Fig. 4(b). The graphs in Fig. 4 show the situation for electrons which reach the central calorimeter under normal incidence (electrons produced at pseudo-rapidity $\eta = 0$). The central calorimeter covers the region $|\eta_{detector}| < 1.2$, where $\eta_{detector}$ is defined with respect to the nominal interaction point. But since the luminous region of the Tevatron is long (1.2 metres), electrons that reach the central calorimeter can be produced at rapidity $|\eta|$ up to 1.5. Due to simple geometrical effects, the effective amount of material traversed by electrons at non-normal incidence can be significantly larger than for electrons at normal incidence. Both the position of the maximum of the average shower profile and the size of fluctuations around the average depend on the electron energy.

Given a precise description of the material, and given the ability to precisely simulate EM showers, the average energy loss for electrons can be determined from simulations. The correction factors that are needed to correct the energy of electron clusters calculated from the measured cell energies back to the energy of the incident electron are determined as a function of electron η (not $\eta_{detector}$, as η is a better measure of the angle of incidence on the detector material and the effective amount of uninstrumented material traversed) and as a function of cluster energy. The resulting correction factors are shown in Fig. 5(a). The correction factors are closer to unity than expected from Fig. 4(a) since the cell energies that are input to the cluster reconstruction have already been scaled up (using a fixed weight per read-out layer) to take into account part of the energy lost in the uninstrumented material. The weight applied to the first two layers (EM1 and to a lesser extent EM2) is particularly high, which results in an improvement in the electron energy resolution (large energy deposits in the first layers typically imply large energy losses in front of the calorimeter). The electron energy resolution nevertheless exhibits a strong η-dependence (c.f. Fig. 5(b)).
A precise determination of the energy-dependence of the energy correction factors shown in Fig. 5(a) is critical for precision measurements like for example the measurement of M_W. In this measurement, the final calibration of the absolute electron energy scale is performed using the $Z \to e^+e^-$

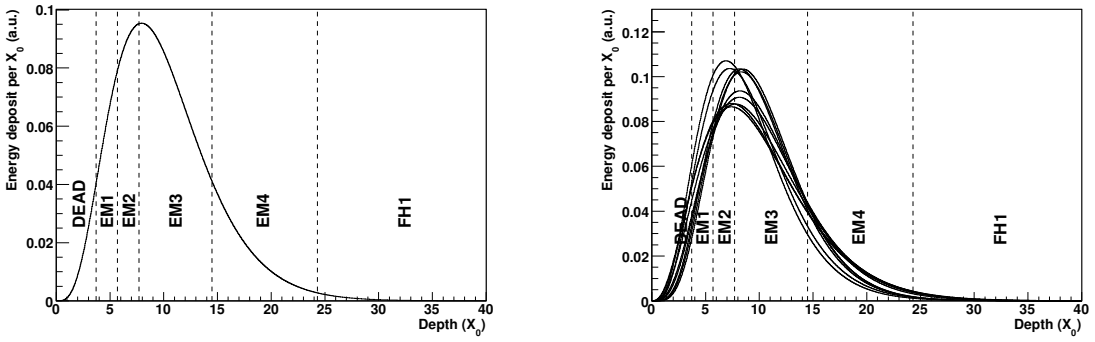

(a) Average longitudinal profile of a shower from an electron with $E = 45$ GeV at normal incidence on the central calorimeter.

(b) Longitudinal profile of ten showers of electrons with $E = 45$ GeV at normal incidence on the central calorimeter.

Figure 4: Illustration of the the importance of uninstrumented material (from the point of view of calorimetry) in the measurements of electron energies with the central calorimeter. The longitudinal shower profiles, including fluctuations, have been taken from the GFlash parameterisation [8]. The readout sections of the central EM calorimeter (EM1 - EM4) and the first section of the fine hadronic calorimeter (FH1) are also indicated.

mass peak, i.e. the DØ measurement of M_W is effectively a measurement of the ratio of the W and Z boson masses which, together with the precise determination of the Z boson mass from LEP is translated into a measurement of M_W. Electrons from Z decay on average carry larger energies than electrons from W decay, so the extrapolation of the electron energy scale from the Z events to the lower energies in W events is a key aspect of the measurement. Therefore a lot of effort has gone into improving the simulation of EM showers in a dedicated version of the DØ simulation program. The key improvements are an update of the parameterisations of the cross sections for EM processes in GEANT3[1], adjustments to the default particle tracking parameters in GEANT3 to force the simulation of individual Coulomb scatters for low-energy electrons (below ~ 500 keV) where Molière theory is no longer applicable, and an adjustment of the amount of uninstrumented material. The amount of uninstrumented material has been adjusted using a comparison of the fractional energy deposits (the contributions per EM layer divided by the total cluster energy) in collider data and in simulation, using electrons from $Z \to e^+e^-$. As can be seen from Fig. 4(a), the faction of electron energy deposited in EM1 and EM2 is very sensitive to the amount of uninstrumented material. The default DØ simulation underestimates the average amount of material in front of the central calorimeter by $(0.1633 \pm 0.0095)\, X_0$. More details of these studies can be found in Ref. [9].

4. Effect and simulation of pile-up effects

When the Tevatron reached its Run II design instantaneous luminosity after the first few years

[1]The parameterisations used in recent versions of GEANT4 are significantly more precise than in GEANT3.

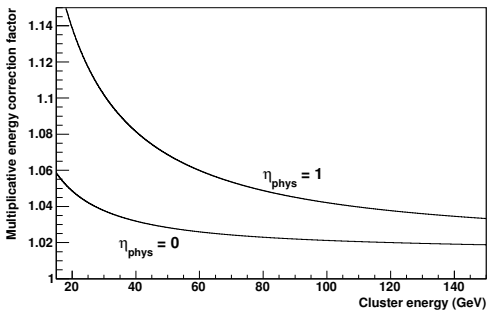

(a) Correction factors used to obtain the electron energy from the energy of the reconstructed electron cluster. The correction factor is shown as a function of cluster energy, for two values of electron η (denoted as η_{phys} in the figure).

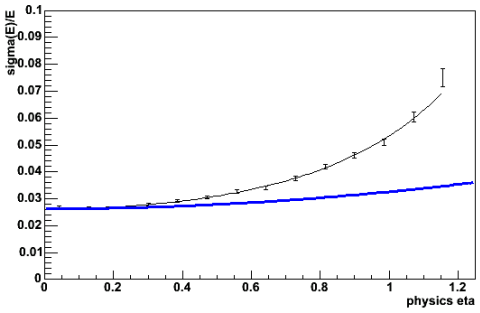

(b) Fractional energy resolution $\sigma(E)/E$ for electrons with energy $E = 45$ GeV detected in the central calorimeter as a function of electron η. The black points are obtained from simulation, the blue line shows the $1/\sqrt{\sin(\theta)}$ dependence that is expected from only the effective change of the thickness of the liquid argon gaps at non-normal incidence.

Figure 5: Correction factors needed to estimate the electron energy based on the measured cluster energy (a), and η-dependence of the electron energy resolution (b).

of operation, the effects of pile-up (additional $p\overline{p}$ interactions occurring during the same beam crossing as the hard $p\overline{p}$ scatter that produced an event of interest [“in time"], or during previous beam crossings [“out of time"]) became important. The instantaneous luminosities delivered by the Tevatron are of course not at the level that is expected at the next generation of colliders, the LHC, nor at the level that has been achieved during the first data-taking campaign of the LHC. But one has to keep in mind that the bunch-crossing time at the Tevatron (396 ns) is significantly longer than at the LHC. For a given instantaneous luminosity, a longer bunch-crossing time implies more (anti-)protons per bunch and therefore large in-time pile-up.

The impact of pile-up in physics analysis is further amplified by the following effect. The mechanical design of the cells of the DØ calorimeter (which impacts cell capacitances etc.) is not optimal for the relatively short signal integration time in Run II, which results in relatively high levels of electronics noise. These noise levels are quantified in Tab. 1. To mitigate this effect, a so-called zero-suppression algorithm is run before the reconstruction of calorimeter objects (electrons, jets, etc): energy measurements from cells which are not above 4σ (c.f. Tab. 1) are discarded, except for cells which have a neighbouring cell that is above the 4σ cut, for which the threshold is reduced to 2.5σ. Cells with negative energy measurements (caused by noise fluctuations, and more importantly, by the effect non-zero energies in the previous crossing which after signal processing results in a negative energy contribution to the current crossing) are also rejected.

The combination of pile-up and zero-suppression has many effects in physics analyses, especially in precision measurements. Here we only have space for one quantitative example, shown in Fig. 6. We consider the energy response of the calorimeter to the hadronic recoil in Z events. At the Tevatron, Z bosons are typically produced with a finite transverse momentum p_T; the peak of the transverse momentum distribution is below $p_T = 10$ GeV. The transverse momentum of the Z boson

is balanced by a set of hadrons recoiling against the Z. These hadrons are typically produced by QCD radiation off the initial state quarks that produce the Z, and the recoil p_T is typically carried by multiple particles, i.e. the p_T per final-state particle is even smaller than the boson p_T. Figure 6 shows the energy response[2] for the hadronic recoil, as obtained from simulation. These results are obtained using only the standard cell-level gain calibrations, which are optimised for high-p_T electrons (i.e. the fractional energy response for electrons after the cell-level calibrations is close to unity, with significant dependencies on the angle of incidence and the energy of the electron, c.f. Sec. 3). No corrections for the effects of uninstrumented material in front of the calorimeter or for the expected differences in energy response for hadrons compared to electrons or for neutrinos and muons in the hadronic recoil are applied here. We note that even at high Z boson p_T the energy response for the hadronic recoil is significantly lower than for high-p_T electrons. The response for the hadronic recoil is particularly low at low recoil p_T where the effect of uninstrumented material dominates. Another important point to note in this figure is the difference in energy response for the hard recoil predicted by simulations with and without the effect of pile-up. The first simulation does not include pile-up at all. In the second simulation, the effect of pile-up is included using a technique we call “ZB overlay", which has become the standard in the simulations for Run II physics analyses. In the DØ simulation, the hard scatter is simulated using an event generator[3], and the resulting final state particles are processed through a simulation of the DØ detector based on the GEANT toolkit, as is common in high-energy physics experiments. Contributions from pile-up can be simulated using the same approach: use an event generator and GEANT to simulate multiple soft $p\overline{p}$ interactions, and add the expected number of additional soft interactions to the event; given a precise model of the signal shaping and readout, the effect of out-of-time pile-up can be included in a similar way. While this procedure is available as an option in the DØ simulation software, the simulated samples used in Run II physics analyses use a different approach to model pile-up. To take into account pile-up, a zero bias (ZB) event from collider data is overlaid on the simulated hard scatter. As discussed before (Sec. 2), zero bias events are collected during normal collider data taking by triggering the detector readout and data acquisition on randomly selected beam crossings. For the calorimeter, “overlaying" a ZB event on a simulated hard scatter means adding, separately for each readout cell, the energy deposits measured in the ZB event to the simulated energy deposits from the hard scatter. This technique allows us to include the effects of pile-up and noise, as seen in data, in the simulated samples. During normal physics data taking, DØ routinely recorded ZB events at a rate of ~ 2 Hz using the normal configuration of the readout electronics (which includes a zero-suppression cut at 1.5σ; the more strict suppression discussed above is only applied in the reconstruction software), plus ~ 1 Hz without zero suppression. The importance of the 1.5σ zero suppression in the collection of the ZB data depends on the goal of a

[2]For the bulk of the Z events, the final state hadrons that constitute the hadronic recoil in a given event are spread out over a large area in the detector. Narrow jets of particles only appear at higher Z transverse momentum in the high part of the spectrum in Fig. 6. In this study, we calculate the combined p_T of the energy deposits from the recoiling hadrons, and we project it on the expected direction of the hadronic recoil (opposite the Z in the transverse plane). The quantity labelled “fractional energy response" is the ratio of the measured projected p_T over the expected p_T (which is equal to the p_T or the Z boson).

[3]For example PYTHIA, but many other generators are available in the literature and have been interfaced to the DØ simulation software.

given simulated sample. If the goal of the simulation is to describe backgrounds in, say, a search for new physics in a final state with tens or hundreds of GeV of missing transverse energy, then this minimal zero suppression has little effect. If the goal of the simulation is to study the energy response to low-p_T particles (like e.g. in Fig. 6), then impact of the energy deposits lost due to the 1.5σ cut would be appreciable. This is why the sample of ZB events collected without zero suppression is used for the latter kind of studies, including the one shown in Fig. 6.
To obtain the curve with ZB overlay in Fig. 6, the energy contributions from the ZB event alone (after the full software zero suppression) have been subtracted from the cell energies in the full simulated event (hard scatter plus overlay of ZB event collected without zero-suppression; the standard software zero suppression algorithm is applied on the sum of simulated and ZB energies). This means that the significant increase in recoil energy response that is observed compared to the simulation without pile-up is caused by the following effect: energy deposits in a given cell of the calorimeter from the hard scatter and deposits from the ZB event in the same cell would each individually fail the zero suppression cut, but the sum of the two deposits passes the zero suppression threshold.

Layer	σ [ADC counts]	σ [MeV]
CC-EM1	3.1	48
EC-EM1	3.2	50
CC-EM3	2.0	25
CC-FH1	6.6	80
CC-CH	6.4	297

Table 1: Typical noise levels (from electronics, uranium decay) per read-out cell, as measured from “pedestal runs" (read out detector in the absence of beam).

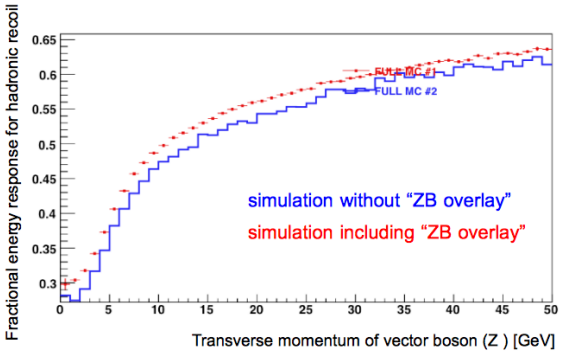

Figure 6: Fractional energy response for the hadronic recoil in $p\overline{p} \to Z+X$ events as measured from simulated events. The results obtained from two different simulations are shown: one simulation (red curve) does not include the effect of pile-up, whereas the the other one (blue curve) includes the effect of pile-up using the “ZB overlay" technique.

The effect discussed above leads to non-trivial luminosity- (pile-up-) dependencies of the energy response to the hadronic recoil, and also of the contributions of pile-up to the measured electron energies. Precise measurements of the electron and recoil energies are key ingredients of the DØ measurement of the W boson mass which is based on $p\overline{p} \to W+X \to e\nu+X$ events. The combination of detailed simulations of the hard scatter based on GEANT and the pile-up based on ZB overlay provide a critical tool that is used to quantify these effects. The $Z \to e^+e^-$ control sample (using the position of the mass peak for the electrons, and the observed imbalance of the hadronic recoil and the di-electron system for the recoil) allows for final verifications of the predictions using events from collider data that are similar to the signal W events.

5. Conclusions

During Run II, the DØ calorimeter had to operate under much more difficult conditions than during Run I. This lead to significant challenges, some of which were expected and others were not. The main challenges are due to the large instantaneous luminosity in Run II (which results in a shorter integration time and larger pile-up) and the large increase of the amount of uninstrumented material in front of the calorimeter. We have summarised some of these challenges and the solutions that have been implemented to overcome them. In the end, the energy resolution is necessarily not as good as in Run I (e.g. the sampling term in the electron energy resolution of the central calorimeter [averaged over the η/energy spectrum of electrons from $Z \to e^+e^-$] has been increased from 15 % to 21 %, and the constant term has been increased from below 1 % to (1.997 ± 0.073) %), but the resolution in Run II is still consistent with the physics goals. More importantly, calorimeter energy scales for all kinds of objects (including their dependencies on rapidity, instantaneous luminosity, ...) are precisely quantified and understood. This is one of the bases of the rich collection of physics results from DØ in Run II. In this article we have only discussed two of the most difficult analyses, namely the measurements of the top quark and W boson masses, but the techniques developed in this context also bear fruit in many other analyses.

Acknowledgments

The speaker would like to thank the organisers and all participants for this exciting and informative conference, and all members (past and present) of the DØ Collaboration for the fruitful and pleasurable collaboration over all these years.

References

[1] G. Aad et al. Observation of a new particle in the search for the Standard Model Higgs boson with the ATLAS detector at the LHC. *Phys.Lett.*, B716:1–29, 2012.

[2] S. Chatrchyan et al. Observation of a new boson at a mass of 125 GeV with the CMS experiment at the LHC. *Phys.Lett.*, B716:30–61, 2012.

[3] S. Heinemeyer, W. Hollik, and G. Weiglein. Electroweak precision observables in the minimal supersymmetric standard model. *Phys.Rept.*, 425:265–368, 2006.

[4] S. Heinemeyer, W. Hollik, D. Stockinger, A.M. Weber, and G. Weiglein. Precise prediction for M(W) in the MSSM. *JHEP*, 0608:052, 2006.

[5] L. Zeune et al. To appear. 2013.

[6] CDF and DØ Collaborations. Combination of CDF and DØ W-Boson Mass Measurements. *arXiv:1307.7627*, 2013.

[7] V.M. Abazov et al. The Upgraded D0 detector. *Nucl.Instrum.Meth.*, A565:463–537, 2006.

[8] G. Grindhammer, M. Rudowicz, and S. Peters. The Fast Simulation of Electromagnetic and Hadronic Showers. *Nucl.Instrum.Meth.*, A290:469, 1990.

[9] J. Stark. Mise au point de la calorimétrie au Run II de l'expérience DØ et mesure de la masse du boson W (in French). Habilitation thesis. University Joseph Fourier, Grenoble, France. 2013.